





**FULL ARTICLE**

# 3D-Printed high-NA catadioptric thin lens for suppression of XPM background in Stimulated Raman Scattering microscopy

Andrea Bertoncini  | Sergey P. Laptенок  | Luca Genchi  |  
Vijayakumar P. Rajamanickam | Carlo Liberale\* 

Biological and Environmental Science and Engineering Division (BESE), King Abdullah University of Science and Technology (KAUST), Thuwal, Saudi Arabia

**\*Correspondence**

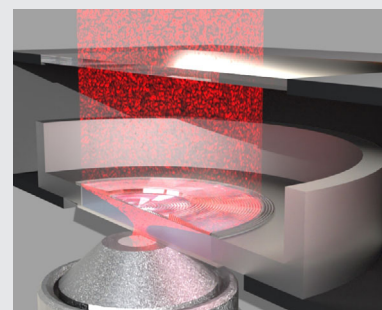
Carlo Liberale, Biological and Environmental Science and Engineering Division, King Abdullah University of Science and Technology (KAUST), Thuwal, Saudi Arabia.  
Email: carlo.liberale@kaust.edu.sa

**Funding information**

Global Collaborative Research, King Abdullah University of Science and Technology, Grant/Award Number: ORS-2016-CGR5-3017

**Abstract**

Stimulated Raman Scattering (SRS) is a fast chemical imaging technique with remarkable bioscience applications. Cross Phase Modulation (XPM) is a ubiquitous nonlinear phenomenon that can create spurious background signals that render difficult a high-contrast imaging in SRS measurements. The XPM-induced signal is usually suppressed using high numerical aperture (NA) microscope objectives or condensers to collect the transmitted excitation beam. However, these high NA optics feature short working distances, hence they are not compatible with stage-top incubators, that are necessary to perform live-cell time-lapse experiments in controlled environments. Here, we show a 3D printed high NA compact catadioptric lens that fits inside stage-top incubators and allows the collection of XPM-free SRS signals. The lens delivers SRS images and spectra with a quality comparable to a signal collection with a high-NA microscope objective. We also demonstrate the compatibility of the 3D printed lens with other nonlinear microscopies usually associated with SRS in multimodal microscopes.


**KEYWORDS**

3D printing, micro-optics, multi-photon microscopy, stimulated Raman scattering microscopy

## 1 | INTRODUCTION

Stimulated Raman Scattering (SRS) microscopy is a label-free chemical imaging technique with compelling applications in biology and medicine [1], including single-cell metabolism [2–5], neuroscience [6], and tissue histology [7, 8]. Thanks to their intrinsic optical sectioning capability, SRS microscopes can map the three-dimensional distribution of chemical bonds within a sample, with a

sensitivity that allows video-rate imaging of biological specimens [9]. SRS occurs when molecular vibrations are coherently driven by two laser beams at different wavelengths, overlapped in space and time, and whose difference in optical frequencies corresponds to vibrational modes of the molecules. In such event, the driven coherent molecular vibration mediates a transfer of energy between the two beams, for which the shorter-wavelength beam (pump beam) experiences a loss of intensity

(Stimulated Raman Loss), while the longer-wavelength beam (Stokes beam) experiences an increase of intensity (Stimulated Raman Gain, SRG). The relative change of the intensity due to the SRS effect is very small ( $\Delta I/I \sim 10^{-4} \div 10^{-6}$ ), hence SRS setups implement a detection scheme based on high-frequency modulation transfer to overcome the relatively high laser noise at low frequencies [10]. In such a detection scheme, one of the two beams is amplitude-modulated and a lock-in amplifier or a tuned amplifier that [11] retrieves the relative laser intensity modulation induced on the other beam. This detection configuration enables a suitable signal-to-noise ratio in SRS measurements but can lead to the detection of spurious signals if the electronic and optical setups are not correctly implemented.

In particular, the cross-phase modulation (XPM) is a nonlinear transient scattering effect that can introduce artifacts in SRS measurements [12, 13]. XPM has a non-resonant electronic origin; therefore, it does not provide any chemical information. The XPM effect occurs when two intense beams interact—as in the SRS scheme—and transiently change the refractive index of the material due to its ubiquitous third-order nonlinear optical susceptibility. The instantaneous and intensity-profile-dependent modulation of the refractive index, seen by one beam as a result of the other beam, induces a transient change of the angular divergence of the two beams after passing through the sample. In a SRS setup, this variation of the beam divergence has the same temporal pattern as the amplitude-modulated beam. When the optical detection path does not collect the full numerical aperture (NA) of the beam to be measured, the XPM-related beam divergence variation translates into a beam power variation at the photodetector. This optical power fluctuation is detected by the lock-in amplifier and is indistinguishable from the real Raman signal from the sample, becoming a spurious background contribution to the measured signal. Moreover, this background contribution added by XPM depends on the local nonlinear properties of the sample, so it varies point by point and cannot be easily subtracted in SRS images. For this reason, most SRS setups reported in the literature use collection optics having a higher NA than the excitation optics to suppress the background signal caused by XPM [14].

SRS microscopy is a powerful technique to perform label-free imaging of live cells, which requires to maintain suitable culture conditions with the use of an incubator [15]. In particular, stage-top incubators are the solution of choice when performing live-cell time-lapse experiments with fast-changing environmental parameters (temperature, humidity, oxygen level, and so on) thanks to the small volume of their chamber. Moreover, stage-top incubators avoid the exposure of critical parts

of the equipment (e.g., electronics) to high-humidity environments. Conversely, cage incubators enclose the entire microscope and have higher inertia in controlling environmental parameters. Typically, the closed chamber of a stage-top incubator has a few centimeters height and a transparent window to allow a transmission path for the light. However, high NA objectives or condenser lenses—needed in collection to avoid XPM-related background in SRS microscopy—usually have a millimeter or lower working distance, therefore they are incompatible with stage-top incubators in inverted microscopes. A solution for high NA collection with stage-top incubators has been used by Lu et al [15] for an upright microscope. They have customized a top-stage incubator by using a flexible plastic top cover that allows fitting the excitation high NA objective inside the incubator chamber. While a similar solution could be potentially used with an inverted microscope, the needed customization is not generally possible for all stage-top incubators. Additionally, this solution makes it difficult or impossible to navigate across the sample by moving the microscope stage. The reduction of the XPM signal in SRS microscopy can also be achieved with special detection schemes based on polarization modulation [13], frequency modulation [12, 16] or SRG and Opposite Loss Detection (SRGOLD) [17, 18]. However, these solutions require a substantial modification to the optical setup or custom components.

Here, we present a high NA 3D printed condenser thin-lens that fits inside a stage-top incubator and efficiently directs an otherwise highly divergent beam to a photodetector. This lens has a catadioptric design, that is, it is made by both refractive and reflective optical elements to achieve a high NA. The refractive elements are in the center of the lens and collect the low-divergence part of the beam, while the reflective elements are in the outer part of the lens and collect the high-divergence part of the beam. By using this lens, we could measure XPM-free SRS spectra from cells in a stage-top incubator. Our results also imply that our 3D printed lens can replace a bulky and expensive high-NA microscope objective for forward signal collection in point-scanning microscopies.

## 2 | METHODS

### 2.1 | Design of the catadioptric lens

In point-scanning laser-based microscopes, such as SRS, a laser beam is focused and scanned across the sample, and the signal is detected, point-by-point, with a single bucket photodetector. The images are then digitally reconstructed pixel by pixel. In such configuration, the main purpose of detection optics is to collimate a

divergent beam and to direct it to the photodetector. Hence, the collection optics does not require imaging capabilities. Therefore, we designed the catadioptric lens using ray tracing calculations, in the context of nonimaging optics [19], where the aim is the maximum transfer of optical power between the source and the detector. Moreover, as our main application is the imaging of biological samples in aqueous solutions, the lens was designed to work in water immersion. The design of the lens is sketched in Figure 2A and, in its working principle, is similar to the one of lighthouse Fresnel lenses [20] in which an isotropic light source (i.e., a torch) was collimated to signal the presence of land to ships far away. The complete structure of the designed lens incorporated a 170  $\mu\text{m}$  thick glass slab, corresponding to a standard microscope coverslip #1,5 (Figure 1A), used as the substrate for the lens fabrication. The NA was set to 1.2, while the working distance was chosen to be 1.35 mm, equal to the measured depth of the well in a glass bottom petri dish (Nunc<sup>TM</sup> Glass Bottom Dishes, Thermo Scientific) (Figure 1D). In this way, after the petri dish well is filled with an aqueous solution, such as cell culture medium, and the lens placed on top, capillary forces fix the position of the lens, and the well depth defines the working distance. With these values for the working distance and desired NA parameters, the minimum diameter of the collimating catadioptric lens is about 6 mm.

The refractive part of the lens had a Fresnel-lens design—corresponding to a segmented spherical lens—and collimated the innermost, low NA part of the beam, up to 0.74 NA (in water immersion). The design of the reflective part of the lens, showed in cross section in Figure 1A, was composed of many slanted parallelograms that redirected the rays upward by one total internal reflection. The inclination angle of these parallelograms varied with the radial position and was calculated with a script based on geometrical optics. Remarkably, the working distance of the designed lens can be adjusted by a simple isotropic scaling of its profile. The height for both the refractive and reflective elements of the lens was less than 100  $\mu\text{m}$  which, combined with the thickness of the coverslip (170  $\mu\text{m}$ ), resulted in a 270  $\mu\text{m}$  thick lens that could fit inside narrow spaces, such as a Petri dish.

We designed the catadioptric lens using the 1.35 mm nominal height for the well of the glass bottom petri dish as a reference parameter. While this value is pretty close to the real height of the well, its unavoidable fluctuations in manufactured petri dishes can make critical the exact axial positioning of the lens. Indeed, due to the short focal distance of the catadioptric lens, the beam divergence after the lens is very sensitive to its distance from

the laser focusing position. Therefore, in practical conditions, the fluctuations in the well height can make the beam to be no longer ideally collimated but instead significantly diverging, and becoming larger than the diameter of the final lens ( $f_2$  in Figure 1C), which focuses the beam on the photodetector. Additionally, to ensure the capability to image even thick samples—which can be in the order of 200  $\mu\text{m}$ —a possible shift of the distance of the beam focusing plane with respect to the catadioptric lens should be accounted for. For this reason, in the final design of the whole collection optics system, we included a convex lens ( $f = 30$  mm) positioned just above the glass lid of the stage-top incubator (Figure 1C). This lens compensated the above described effects on the variation of beam divergence after the catadioptric lens, so that the collection of optical power on the photodetector remained unaffected under normal experimental conditions.

## 2.2 | Fabrication

We fabricated the designed catadioptric lens with a high-resolution additive manufacturing approach. This approach is needed as the reflective section of the catadioptric lens (Figure 1A) features microscopic slanted cuts that have to be reproduced with high accuracy in order to create the total internal reflection surfaces. Such small and slanted cuts would be challenging to reproduce with other traditional fabrication methods. The refractive section of the lens is also composed by microscopic features that require a high-precision fabrication method to generate surfaces with good optical quality. We used high-resolution 3D printing based on two-photon lithography [21] that has established itself as a groundbreaking solution for the fabrication of polymeric micro-optical elements, with many recent successful examples [22–25]. The high-precision 3D fabrication provided by this method uniquely meets the demands set by the microscopic features of the refractive and the reflective sections of the catadioptric lens. We used a commercial two-photon lithography system (Nanoscribe Photonic Professional, Nanoscribe GmbH) with their proprietary photoresist IP-S (Nanoscribe GmbH, Germany) in Dip-in configuration [22]. The IP-S photoresist provides smooth surfaces and fast fabrication of relatively large volumes, so it is indicated for the manufacturing of micro-optics. We used a shell-and-scaffold fabrication approach to minimize the printing time of the lens, without compromising on the surface smoothness by using a 300 nm slicing fabrication parameter. The fabrication was followed by a postdevelopment UV curing to polymerize the bulk of the structure. With this optimized

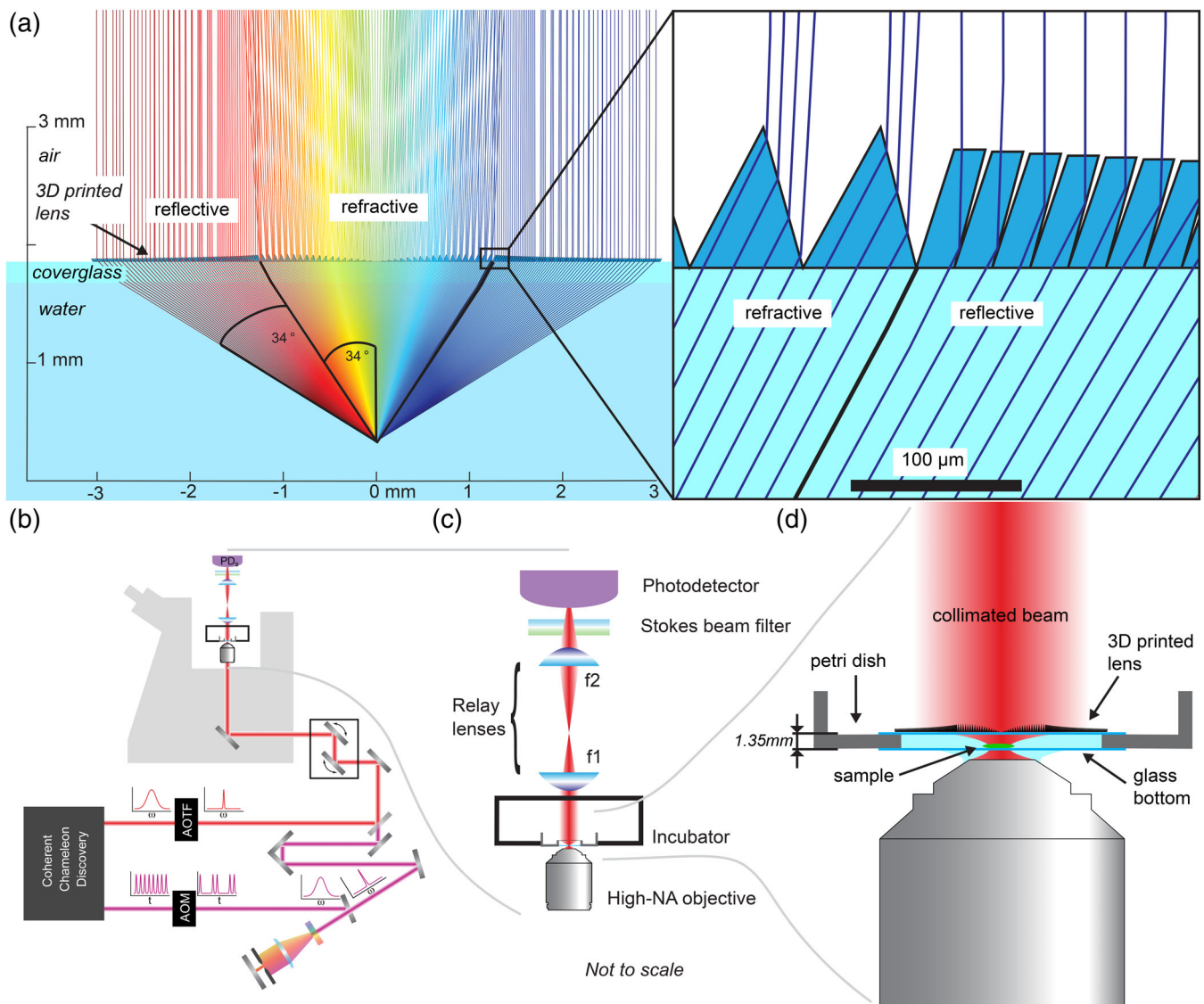


**FIGURE 1** 3D printed catadioptric thin lens design. A, Geometrical optics simulation of the 3D printed lens design. The low numerical aperture (NA) ( $NA < 0.74$ ) part of the beam is collimated by refractive elements, while the high-NA ( $0.75 < NA < 1.2$ ) part of the beam is collimated by reflective elements. B, Optical setup of the SRS microscope used to study the performance of the 3D printed lens. C, Detail on the collection path of the setup.  $f_1$ :  $f = 30$  mm lens;  $f_2$ :  $f = 70$  mm lens; D, Detail on the mounting configuration of the 3D printed lens on a glass bottom petri dish

strategy, the fabrication time of a 1.2 NA lens (Figure 2) was about 4 hours. The fabrication of the lens was done by dividing the total 6 mm diameter area in smaller hexagonal zones with a long diagonal of about  $500 \mu\text{m}$ , corresponding to the maximum area that can be fast-printed based on galvanometer scanners. The entire lens was then realized by the sequential printing of each individual zone, allowed by the mechanical positioning stage of the printing machine. This large-area fabrication strategy leads to “stitching” defects [26] that are generated by the stage backlash error and are visible as a hexagonal pattern in the Scanning Electron Microscopy (SEM) image of Figure 2.

### 2.3 | SRS setup

We characterized the 3D printed lenses on a home-build SRS microscope that is described by Laptinok et al [4]. The setup is sketched in Figure 1B. The laser source is a commercial Optical Parametric Oscillator pumped by a femtosecond fiber-laser featuring two 80 MHz temporally synchronized outputs (Chameleon Discovery, Coherent Inc.). One output has a fixed wavelength (1040 nm, 2.5 W average power), and acts as the Stokes beam, while the second output is tunable between 680 and 1300 nm and acts as the pump beam. In the wavelength range used during the experiments (780–950 nm),



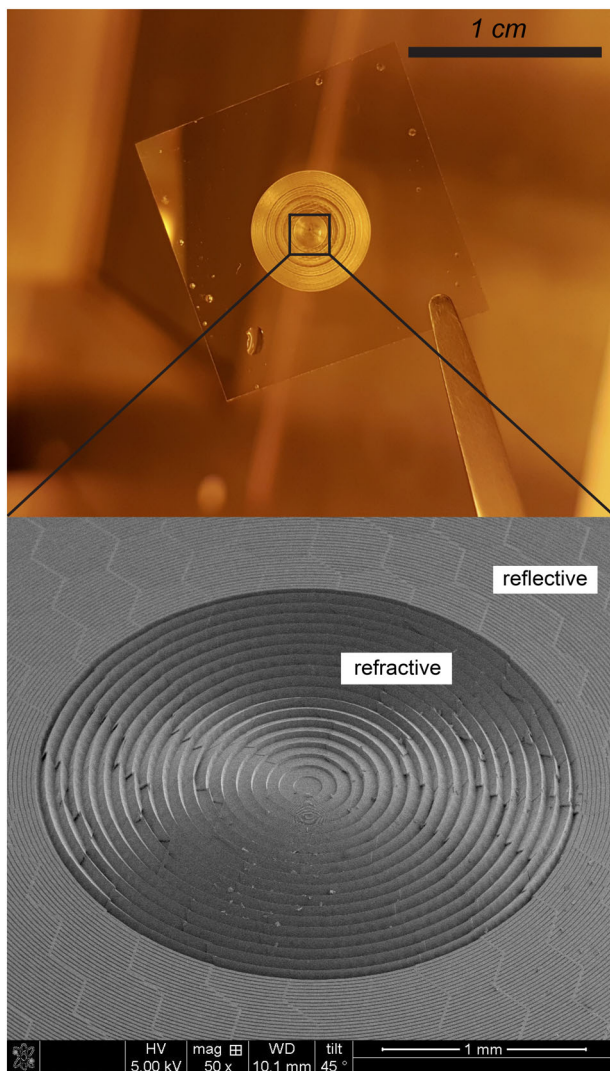


**FIGURE 2** Images of the 3D printed lens (top). Optical image of the lens 3D printed on a glass substrate (microscope coverslip #1,5) (bottom). SEM image of the central part of the lens, showing the central Fresnel-lens-like refractive part and the outer reflective part

the laser delivers an average power  $> 1.8$  W. The Stokes beam is amplitude-modulated at 5 MHz with an Acusto Optic Modulator and spectrally narrowed down to a 1 nm bandwidth. The pump beam wavelength is scanned and spectrally filtered using a high-resolution Acousto-optic tunable filter. The two beams are combined and directed into an inverted microscope (Nikon Eclipse Ti-E) where they are focused on the sample with a high-NA microscope objective (CFI Plan Apo  $\lambda$  40 $\times$  0.95 NA, Nikon or CFI Plan Apo IR 60 $\times$  WI 1.27 NA, Nikon). A couple of galvanometric mirrors allow to scan the beam over the sample, and images are digitally reconstructed from the signal measured by a single point photodiode. This SRS setup can also be used in multimodal configuration to measure Coherent Anti-Stokes Raman Scattering

(CARS), Second Harmonic Generation (SHG), and Two-Photon Fluorescence (TPF) signals.

## 2.4 | Cell culture and imaging

Human hepatocellular carcinoma cells (HepG2, American Type Culture Collection, HB-8065) were cultured in a glass bottom petri dish at 37°C in a humidified incubator with 5% CO<sub>2</sub> supply. The Gibco (Thermo Fisher Scientific) media and reagents were used for cell culture maintenance: Dulbecco's Modified Eagle Medium supplemented with 10% fetal bovine serum, 1% penicillin streptomycin and 1% L-Glutamine. Cells were then fixed with 4% paraformaldehyde and the culture medium was replaced with phosphate-buffered saline solution before imaging.

For SRS imaging, the glass bottom petri dish with the 3D printed lens was inserted inside a stage-top incubator (H101-NIKON-TI-S-ER, Okolab, Italy), whose chamber height allows a minimum condenser working distance of 27 mm.

## 3 | RESULTS AND DISCUSSION

### 3.1 | Rejection of XPM-related background with the catadioptric lens

We tested the 3D printed catadioptric lens by observing the XPM-related background signal in SRS measurements. In particular, we compared the 3D printed lens with other two collection optics, namely a high-NA microscope objective (CFI Apo LWD 40 $\times$  WI  $\lambda$ S 1.15 NA, Nikon) and a 1-inch diameter  $f = 30$  mm lens (0.4 NA, AC254-030-AB, Thorlabs), in combination with a 0.95 NA microscope objective (CFI Plan Apo Lambda 40XC, Nikon) for the focusing of the beams. The high NA objective used in collection acted as a benchmark for the rejection of XPM-related signal; however, it is not compatible with a stage-top incubator due to its short working distance, therefore we used it by removing the lid of the incubator chamber. The convex lens was the available optics with the shortest focal length, and highest NA compatible with the 27 mm height of the used stage-top incubator chamber to perform SRS measurements. Figure 3 shows the SRS spectra of the UV-cured NOA63 photopolymer (Norland Products, Inc) in the region between 2650 and 3150 cm<sup>-1</sup>. The main Raman peak for this material in the CH-stretch region is at about 2930 cm<sup>-1</sup>. The spectral region between 2650 and 2750 cm<sup>-1</sup> is instead a silent region of the vibrational spectrum, therefore any signal measured here is a nonresonant

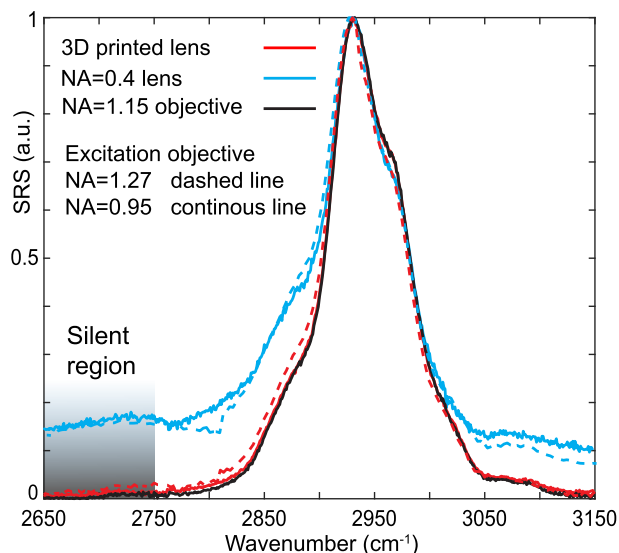


**FIGURE 3** Stimulated Raman Scattering (SRS) spectra with different combinations of excitation and collection optics. SRS spectra in the CH-stretch region for the UV-cured NOA63 photopolymer with different combinations of excitation and collection optics. Continuous and dashed lines correspond to excitation with a microscope objective having 0.95 numerical aperture (NA) and 1.27 NA, respectively. The three different collection optics is: a  $f = 30$  mm 0.4 NA lens (blue lines), a 1.15 NA microscope objective (black line), and the 3D printed catadioptric lens (red lines). The highlighted spectral range is a silent region for the vibrational spectrum of the material

background signal, in this case dominated by the XPM-related effect. The 3D printed lens clearly showed a rejection of the background signal compared to the convex lens, and the rejection was as good as the one provided by the high-NA microscope objective, demonstrating the validity of our approach.

We also evaluated the rejection of the XPM-related background when using our 3D printed lens in combination with a higher NA microscope objective for beam focusing (CFI Plan Apo IR 60x WI 1.27 NA, Nikon). This objective provides better focusing condition to the beams, enhancing the SRS signal and the spatial resolution. As reported in Figure 3, the catadioptric lens outperformed again the  $f = 30$  mm lens, being able to reject most of the background signal, almost to the level of a full-NA collection case (0.95 NA excitation and 1.15 NA collection).

### 3.2 | SRS imaging with the catadioptric lens

To demonstrate the suitability of the catadioptric lens for SRS chemical imaging, we collected SRS images with different collection optics and compared them.

First, to assess possible distortions or uneven XPM-rejection across SRS images, we collected SRS images of a polymeric test grid, created on the coverslip of a glass bottom petri dish, which was filled with water. The test grid was printed with the same high-resolution 3D printer and IP-S photopolymer used to fabricate the catadioptric lens. The images in the top row of Figure 4 were collected at a nonresonant wavenumber ( $2550\text{ cm}^{-1}$ ) for both the photopolymer and water, and showed that with high NA collection optics, such as the microscope objective and the 3D printed lens, the XPM background did not appear. On the other hand, with low NA collection optics (0.4 NA  $f = 30$  mm lens), a strong background was detected both on and outside of the grid lines, due to XPM in water and in the IP-S photopolymer, respectively. The images in the middle row of Figure 4 were instead collected at a resonant wavenumber for the IP-S photopolymer ( $2950\text{ cm}^{-1}$ ), and showed that the 3D printed lens is well suited for SRS imaging while suppressing XPM-related signal. Indeed, the quality of the SRS image collected through the 3D printed lens was comparable to the one collected using the commercial high NA objective, showing a defined grid with consistently low background across the field of view (FOV) of the used excitation objective. Conversely, the image obtained with the 0.4 NA lens at the resonant wavenumber showed a high background between the grid lines, clearly related to XPM. Figure 4C shows SRS images of a HepG2 cancer cell collected at a resonant wavenumber for lipids ( $2850\text{ cm}^{-1}$ ). The round spots with high signal in these images represent lipid droplets inside the cell [27]. Again, the SRS image collected with the 3D printed lens was very similar to the one collected with the high NA objective, while the SRS image obtained with the 0.4 NA lens presented several artifacts and distortions. In particular, the nucleus and the cytoplasm of the cell are visible even though they have no significant resonant components at  $2850\text{ cm}^{-1}$  and the lipid droplets have a nonuniform signal distribution, whose origin is not fully understood, but possibly due to the interplay between XPM and Raman contributions.

### 3.3 | Lateral positioning of the catadioptric lens

Following its optical design, the 3D printed lens was placed on top of the water-filled well at the center of a glass bottom petri dish (Figure 1D). The petri dish was then mounted with a proper holder inside the stage-top incubator. This positioning of the lens is convenient as

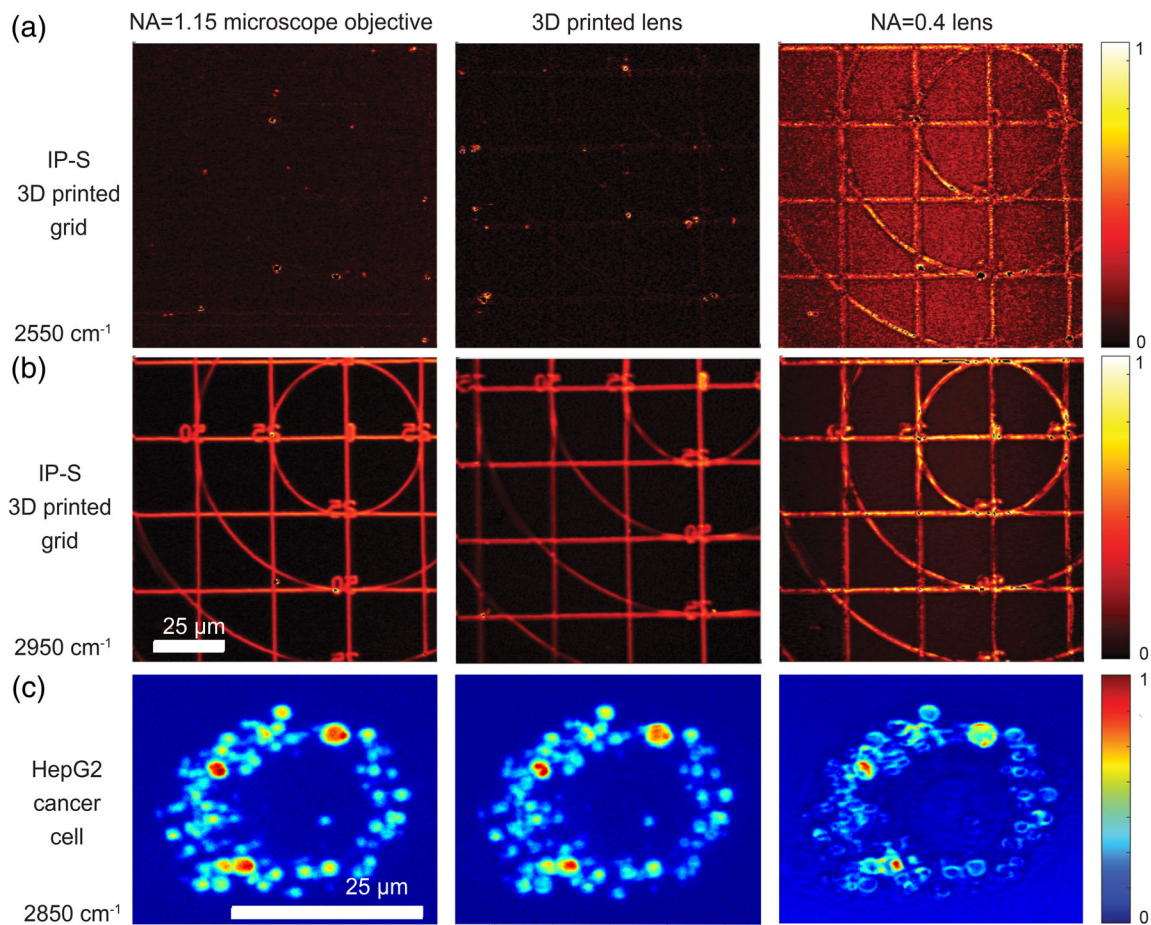


**FIGURE 4** Stimulated Raman Scattering (SRS) imaging with different collection optics. A, SRS images of a IP-S 3D printed grid at a nonresonant wavenumber ( $2550\text{ cm}^{-1}$ ). A strong Cross Phase Modulation (XPM)-related background is visible with the 0.4 NA lens, while it is suppressed with the 3D printed lens and the high NA microscope objective. B, SRS images of the same grid as above at  $2950\text{ cm}^{-1}$  wavenumber, where the photopolymer Raman spectrum has a peak. C, SRS images of a HepG2 cancer cell at  $2850\text{ cm}^{-1}$ , highlighting lipid droplets in the cell. The suppression of XPM-artifacts with 3D printed lens is comparable to the high-NA microscope objective. Excitation was done with the 1.27 NA microscope objective

it does not require any external mount that would be particularly challenging to fit inside the incubator. At the same time, because of this positioning, the catadioptric lens is in joint with the petri dish and loses its alignment with respect to the excitation microscope objective when the microscope stage is translated. If the excitation objective is not perfectly aligned with the optical axis of the 3D printed lens, the collimated output beam is deflected and partially scattered by the edges of the printed microstructures, therefore no longer efficiently relayed to the photodetector. This effectively reduces the area of the sample where the full NA of the excitation beam is collected, leading to a decreased capability in rejecting the XPM-related background in SRS measurements. For this reason, a manual lateral realignment of the catadioptric lens is needed if the sample is laterally translated with the microscope stage. To understand how critical is this

realignment step for the user, we characterized the effect of a lateral offset of the catadioptric lens optical axis. Figure 5 shows the SRS spectra of a  $15\text{ }\mu\text{m}$  thick uniform layer of the UV-cured NOA63 photopolymer in the region between  $2650$  and  $3150\text{ cm}^{-1}$ , as measured by varying the lateral offset between the axis of the catadioptric lens and the axis of the excitation microscope objective. The data show that the XPM-related signal in the silent spectral region remained low for radial offsets up to  $1\text{ mm}$ , meaning that the manual positioning of the lens has a  $\pm 1\text{ mm}$  tolerance, so it is not critical for the user. Of note, this positioning tolerance hints for a large collection FOV for the catadioptric lens, exceeding the FOV granted by the used laser scanning configuration and excitation microscope objectives. This observation is confirmed by the even performances across the FOV allowed by the excitation objective shown in Figure 4B.



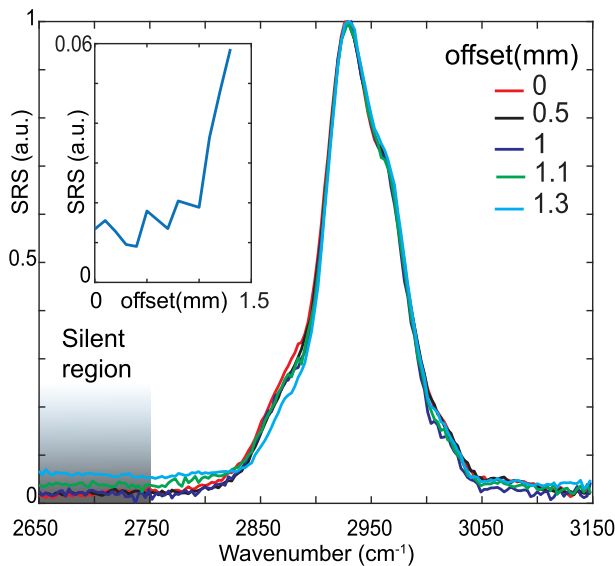


**FIGURE 5** Stimulated Raman Scattering (SRS) spectra at different lateral offsets for the catadioptric lens. SRS spectra of the NOA63 photopolymer at different offsets between the axis of the catadioptric lens and the axis of the excitation microscope objective (1.27 numerical aperture). inset Average SRS signal in the silent region ( $2650\text{--}2750\text{ cm}^{-1}$ ) at different offsets. The SRS signal in the silent region is due to the Cross Phase Modulation (XPM) effect only and increases outside of the working region for the catadioptric lens (offset  $>1\text{ mm}$ )

### 3.4 | Collection efficiency of catadioptric lens

We then tested the collection efficiency for the 3D printed catadioptric lens. Table 1 shows the comparison of the collection efficiencies for the three different optics, obtained by measuring the transmitted optical power at the photo-detector position. The 3D printed lens increases the collection of the signal by a factor of 3.5 with respect to the configuration with the 0.4 NA lens, and reaches almost 80% of what obtained with the 1.15 NA microscope objective.

We note that, while the suppression of the XPM background indicates that the 3D printed lens effectively collects the full NA of the excitation beam, it presents some additional transmission losses with respect to the high NA microscope objective. The losses are mainly due to the intrinsic absorption of the polymerized IP-S material in the near infrared region [28], and to scattering and back-reflection from the many interfaces and small features of the lens. Of note, the fabrication of large area structures with two-photon lithography is affected by the “stitching” problem (see Methods section 2), which is quite evident in the sparse discontinuities in the SEM image in Figure 2. These discontinuities might contribute to additional losses.

### 3.5 | Use of the 3D printed lens with multimodal microscopes

Finally, we tested the potential of the designed catadioptric lens to increase the collection efficiency in other nonlinear microscopy methods with a transmission detection path. This is relevant because SRS microscopes can be easily upgraded to become “multimodal,” implementing also nonlinear methods like CARS, SHG, Third Harmonic Generation (THG), and TPF microscopies [29]. In general, these microscopy methods use high-NA objectives to focus the excitation beam to a small focal volume, obtaining a high local intensity, which enhances the non-linear effects. The large beam divergence induced by high NA objectives poses again a problem if a collection path is needed in forward direction with stage-top incubators. The interest for having a forward detection path can be motivated by the following: in CARS microscopy the signal is mainly directed in the forward direction except for objects smaller than about 50 nm [30]; in SHG microscopy, the ratio of the forward to backward signal gives information on the small-scale morphology of samples [31]; in TPF microscopy, the availability of a forward detection path could allow for another set of dichroic filters and detectors. Figure 6 shows the CARS and TPF measurements performed with forward collection using the catadioptric lens. We compared the catadioptric lens with the  $f = 30\text{ mm}$  lens and with the high-NA microscope objective—serving again as benchmark. Figure 6 shows the forward CARS spectrum of the UV-cured NOA63 photopolymer: the catadioptric lens greatly increases the collected signal, almost to the level of the high NA objective. The fluorescence signal collected by the catadioptric lens in TPF imaging (Figure 6B) of  $10\text{ }\mu\text{m}$  polystyrene fluorescent beads (emission at 515 nm, F8836, ThermoFisher) is very close to what collected by the high NA objective and far higher than what collected by the 0.4 NA lens. Therefore, we demonstrated the compatibility and potential beneficial use of catadioptric lens with multimodal nonlinear microscopes.

## 4 | CONCLUSIONS

We showed the design and high-resolution 3D printing of a thin lens that fits inside stage-top incubators for inverted microscopes, and collects the full NA of beams generated by high NA objectives. The high NA collimation capability is especially relevant in SRS microscopy where a not chemically-specific background signal can arise due to XPM if the collection NA is not sufficiently high. For this reason, we demonstrated the high NA collection of our lens by showing the suppression of XPM-related signal in SRS measurements. The lens showed also satisfying SRS



**TABLE 1** Power collection efficiency of different optics. Comparison of the collection efficiency of the 3D printed lens with respect to the 1.15 NA objective and the 0.4 NA lens. The efficiency was measured as a ratio of the power measured at the position of the photodetector vs the power from excitation objective (1.27 NA)

	Optics	NA	Efficiency
1	1-inch $f = 30$ mm lens	0.4	20%
2	3D printed lens + $f = 30$ mm relay lens	1.2	70%
3	Nikon 40 $\times$	1.15	90%

Abbreviation: NA, numerical aperture.

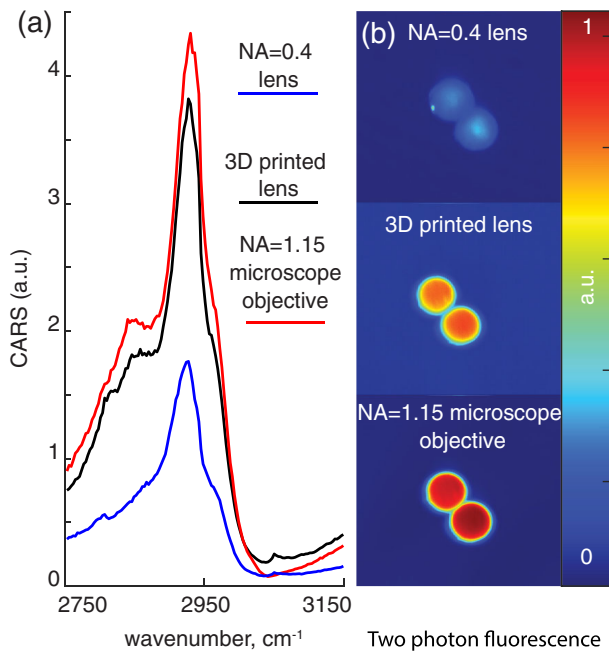


**FIGURE 6** Use of the 3D printed lens for forward signal collection in Two-Photon Fluorescence (TPF) and Coherent Anti-Stokes Raman Scattering (CARS) microscopy. A, CARS spectra of UV-cured NOA63 collected in the forward direction with different optics, showing similar signal intensity for the 3D printed lens and the high numerical aperture (NA) microscope objective. B, TPF imaging of fluorescent plastic beads with different collection optics in the forward direction, showing similar signal intensity for the 3D printed lens and the high-NA microscope objective

imaging capabilities, with no image distortions and an even efficiency across the field of view of a high NA excitation objective. In the context of SRS microscopy, our lens can replace high NA microscope objectives or condensers, whose short focal distance prevents their use in live-cell time-lapse experiments with stage-top incubators. The cost of our lens can potentially be an order of magnitude less than a condenser with comparable NA. Finally, we demonstrated that the proposed 3D printed lens is also beneficial for others high-NA microscopies with a forward collection path, like CARS, and TPF, and it could also

potentially work for other methods, like SHG and THG microscopy.

While collecting the full angular distribution of highly diverging beams, our catadioptric lens showed some additional losses with respect to a high NA microscope objective. This leaves some room for improvement in its collection efficiency. The additional losses could be mitigated by using newer photopolymers for the 3D printing (e.g., PO4 [28]) that feature a lower absorption coefficient. Additionally, we expect that scattering from the proposed lens could be partly reduced by an improvement in the correction of the stitching between different printing areas, or adopting a stitch-less 3D printing system [26]. The scattering from the lens could also be reduced by an improved design of the outer rings in the reflective part of the lens. Indeed, the number of discontinuities seen by the highest angled rays would be reduced by fabricating reflecting elements with a larger base area in that region of the lens. Lastly, the addition of an anti-reflection coating would reduce reflection losses.

The 3D printing fabrication of catadioptric lenses with a higher NA than what shown in this work (1.2 NA) is also possible, at the cost of a longer fabrication time. We expect that the fabrication time will be reduced by future improvements in the 3D printing machines [32].

Beyond the demonstrated application in bioimaging, we foresee that materials science researchers could also benefit from our catadioptric lens for the collection of light from point-emitting sources, like single quantum dots for quantum communications.

## ACKNOWLEDGMENTS

We gratefully acknowledge financial support from King Abdullah University of Science and Technology (KAUST) Office of Sponsored Research (OSR) under Award No. OSR-2016-CRG5-3017.

## ORCID

Andrea Bertoncini  <https://orcid.org/0000-0001-8204-811X>

Sergey P. Laptinok  <https://orcid.org/0000-0002-6468->

3010

Luca Genchi  <https://orcid.org/0000-0002-0808-112X>Carlo Liberale  <https://orcid.org/0000-0002-5653-199X>

## REFERENCES

- [1] F. Hu, L. Shi, W. Min, *Nat. Methods* **2019**, *16*(9), 830.
- [2] R. Long, L. Zhang, L. Shi, Y. Shen, F. Hu, C. Zeng, W. Min, *Chem. Commun.* **2018**, *54*(2), 152.
- [3] J. Garcia-Bermudez, L. Baudrier, E. C. Bayraktar, Y. Shen, K. La, R. Guarecuco, B. Yucel, D. Fiore, B. Tavora, E. Freinkman, S. H. Chan, C. Lewis, W. Min, G. Inghirami, D. M. Sabatini, K. Birsoy, *Nature* **2019**, *567*(7746), 118.
- [4] S. P. Laptinok, V. P. Rajamanickam, L. Genchi, T. Monfort, Y. Lee, I. I. Patel, A. Bertoncini, C. Liberale, *J. Biophotonics* **2019**, *12*(9), e201900028.
- [5] K. Sepp, M. Lee, M. Bluntzer, V. Helgason, A. N. Hulme, V. G. Brunton, *J. Med. Chem.* **2019**, *63*, 2028.
- [6] M. Ji, M. Arbel, L. Zhang, C. W. Freudiger, S. S. Hou, D. Lin, X. Yang, B. J. Bacskai, X. S. Xie, *Sci. Adv.* **2018**, *4*(11), eaat7715.
- [7] D. A. Orringer, B. Pandian, Y. S. Niknafs, T. C. Hollon, J. Boyle, S. Lewis, M. Garrard, S. L. Hervey-Jumper, H. J. L. Garton, C. O. Maher, J. A. Heth, O. Sagher, D. Andrew Wilkinson, M. Snuderl, S. Venneti, S. H. Ramkissoon, K. A. McFadden, A. Fisher-Hubbard, A. P. Lieberman, T. D. Johnson, X. Sunney Xie, J. K. Trautman, C. W. Freudiger, S. Camelo-Piragua, *Nat. Biomed. Eng.* **2017**, *1*(2), 27.
- [8] B. Sarri, F. Poizat, S. Heuke, J. Wojak, F. Franchi, F. Caillol, M. Giovannini, H. Rigneault, *Biomed. Opt. Express* **2019**, *10*(10), 5378.
- [9] B. G. Saar, C. W. Freudiger, J. Reichman, C. Michael Stanley, G. R. Holtom, X. Sunney Xie, *Science* **2010**, *330*(6009), 1368.
- [10] X. Audier, S. Heuke, P. Volz, I. Rimke, H. Rigneault, *APL Photonics* **2020**, *5*(1), 011101.
- [11] C.-S. Liao, M. N. Slipchenko, P. Wang, J. Li, S.-Y. Lee, R. A. Oglesbee, J.-X. Cheng, *Light: Sci. Appl.* **2015**, *4*(3), e265.
- [12] D. Zhang, M. N. Slipchenko, D. E. Leaird, A. M. Weiner, J.-X. Cheng, *Opt. Express* **2013**, *21*(11), 13864.
- [13] M. Andreana, M.-A. Houle, D. J. Moffatt, A. Ridsdale, E. Buettner, F. Légaré, A. Stolow, *Opt. Express* **2015**, *23*(22), 28119.
- [14] C. W. Freudiger, W. Yang, G. R. Holtom, N. Peyghambarian, X. S. Xie, K. Q. Kieu, *Nat. Photonics* **2014**, *8*(2), 153.
- [15] F.-K. Lu, S. Basu, V. Igras, M. P. Hoang, M. Ji, D. Fu, G. R. Holtom, V. A. Neel, C. W. Freudiger, D. E. Fisher, X. S. Xie, *Proc. Natl. Acad. Sci. U. S. A.* **2015**, *112*(37), 11624.
- [16] H. Xiong, N. Qian, Z. Zhao, L. Shi, Y. Miao, W. Min, *Opt. Express* **2020**, *28*(10), 15663.
- [17] P. Berto, E. R. Andresen, H. Rigneault, *Phys. Rev. Lett.* **2014**, *112*(5), 2367.
- [18] A. Lombardini, P. Berto, J. Duboisset, E. R. Andresen, S. Heuke, E. Büttner, I. Rimke, S. Vergnole, V. Shinkar, P. de Bettignies, H. Rigneault, *Opt. Express* **2020**, *28*(10), 14490.
- [19] R. Winston, J. C. Miñano, P. G. Benitez, et al., *Nonimaging optics*, Elsevier, Burlington, MA, **2005**.
- [20] J. Elton, *Int. J. Hist. Eng. Technol.* **2009**, *79*(2), 183.
- [21] H.-B. Sun, S. Kawata, *NMR 3D Analysis Photopolymerization*, Springer, Berlin, **2004**, p. 169.
- [22] T. Gissibl, S. Thiele, A. Herkommer, H. Giessen, *Nat. Photonics* **2016**, *10*(8), 554.
- [23] S. Thiele, C. Pruss, A. M. Herkommer, H. Giessen, *Opt. Express* **2019**, *27*(24), 35621.
- [24] A. Bertoncini, C. Liberale, *IEEE Photonics Technol. Lett.* **2018**, *30*(21), 1882.
- [25] S. Varapnickas, A. Žukauskas, E. Brasselet, S. Juodkakis, M. Malinauskas, *Three-Dimensional Microfabrication Using Two-Photon Polymerization*, Elsevier, **2020**, p. 445.
- [26] L. Jonušauskas, T. Baravykas, D. Andriječ, T. Gadišauskas, V. Purlys, *Sci. Rep.* **2019**, *9*(1), 1.
- [27] L. Tirinato, C. Liberale, S. Di Franco, P. Candeloro, A. Benfante, R. La Rocca, L. Potze, R. Marotta, R. Ruffilli, V. P. Rajamanickam, M. Malerba, F. De Angelis, A. Falqui, E. Carbone, M. Todaro, J. Paul Medema, G. Stassi, E. Di Fabrizio, *Stem Cells* **2015**, *33*(1), 35.
- [28] M. Schmid, D. Ludescher, H. Giessen, *Opt. Mater. Express* **2019**, *9*(12), 4564.
- [29] S. Yue, M. N. Slipchenko, J.-X. Cheng, *Laser Photonics Rev* **2011**, *5*(4), 496.
- [30] J.-X. Cheng, X. S. Xie, *Coherent Raman Scattering Microscopy*, CRC Press, Boca Raton, **2016**.
- [31] M.-A. Houle, C.-A. Couture, S. Bancelin, J. Van der Kolk, E. Auger, C. Brown, K. Popov, L. Ramunno, F. Légaré, *J. Biophotonics* **2015**, *8*(11–12), 993.
- [32] S. K. Saha, D. Wang, V. H. Nguyen, Y. Chang, J. S. Oakdale, S.-C. Chen, *Science* **2019**, *366*(6461), 105.

**How to cite this article:** Bertoncini A, Laptinok SP, Genchi L, Rajamanickam VP, Liberale C. 3D-Printed high-NA catadioptric thin lens for suppression of XPM background in Stimulated Raman Scattering microscopy. *J. Biophotonics*. 2020;e202000219. <https://doi.org/10.1002/jbio.202000219>